



DESIGN AND SIMULATION OF PIEZOELECTRIC MICROCANTILEVER BEAM FOR THE APPLICATION OF COCHLEAR IMPLANT

Md. Zia Khurshid^{1*}, Goutam Chakraborty¹

Abstract

The development of piezoelectric cantilever beams for cochlear implants has gained significant momentum in recent times. This study focuses on the implementation of a piezoelectric material, PZT-8, which is coated with Al₂O₃ and parylene C on both sides. The proposed model incorporates three electrodes made of Ti/Pt material to obtain the output voltage. The dimensions and structure of the cantilever beams were adopted from a previous project, which included four different configurations. A simulation procedure is utilized to evaluate the displacement, output voltage, and Sound Pressure Level (SPL) of each beam. Additionally, the resonance frequency, Q-factor, and Electromechanical Coupling Coefficient (EMCC) are calculated for each beam and compared with previous studies. Moreover, the proposed model's displacement in both water and air environments is simulated, and the resulting output is obtained as deformation due to stress. In comparison to the existing model, the proposed model utilizing PZT-8 material demonstrates superior performance in terms of resonance frequency and Q-factor.

Keywords: Multi-Layered Piezoelectric Microcantilever Beam; Cochlear Implant; Dynamic Response; COMSOL Multiphysics; Electromechanical Coupling Coefficient.

^{1*}Department of Mechanical Engineering, Indian Institute of Technology, Kharagpur, India,
Email: ziakhurshid1@gmail.com; goutam@mech.iitkgp.ac.in

***Corresponding Author:** Md. Zia Khurshid

*Department of Mechanical Engineering, Indian Institute of Technology, Kharagpur, India,
Email: ziakhurshid1@gmail.com, contact: +91 7890088199

DOI: 10.48047/ecb/2023.12.si10.0014

1. Introduction

Micro Electromechanical Systems (MEMS) technology is maturing, and new applications, including consumer items, automotive, and medical applications, are becoming increasingly appealing for research and development. Bulk and surface micromachining are two fabrication approaches of MEMS [1,2]. Several sensor methodologies have been applied by combining these approaches with the deposition of high-quality thin-film materials. The utilization of thin films deposited at low temperatures ($T_b = 300^\circ\text{C}$) allows for the use of a variety of substrates, including metal, glass, plastic, and biocompatible materials. Sensing vibration in the middle ear with a MEMS accelerometer is a biological application that our group is particularly interested in [3]. This approach has been investigated as part of an effort to develop auditory prostheses, improve sensing, and make these systems implantable. The disparity in sound localization offered by the outer ear and ear canal is caused by this sensor arrangement. Cochlear implants (CIs) use electronic devices such as a sound processor, microphone, transmitter, and implant, to restore hearing in people who have severe to profound hearing loss [4].

Digital signal processing (DSP) techniques are used in commercially available cochlear implants (CIs) to deconstruct an input microphone signal into several frequencies filtered bands, which are sent to an electrode array placed in the Scala tympani (ST). However, they have several downsides that limit their everyday use, such as the need for frequent battery replacement/charging, the risk of external components being damaged, particularly if exposed to water (shower, rain), the expensive cost, and patients' aesthetic concerns. The price of the CI could be decreased by mass producing it with microelectromechanical systems (MEMS) technology [5], and other difficulties can be addressed by removing the external unit and the power-inefficient inductive link, resulting in a wholly implanted cochlear implant (CICI). As a result, these characteristics must be met to eliminate the need for a piece of external equipment, such as a sound processor, battery, transmitter, and microphone, which are commonly found in semi-implantable hearing aids.

Even though piezoelectric devices have been suggested as possible options for CI applications [6,7,8], Mechanical vibrations are converted directly into electricity without the necessity of an external source using piezoelectric transducers [9]. Because of these materials' strong piezoelectric activity, piezoelectric actuation allows for more

design flexibility, requires less voltage (as opposed to electrostatic devices) or power [10,11] (as compared to thermal actuators), and produces larger strokes per electrical energy input. Faster and more precise inkjet printheads, faster and less power-hungry autofocus lenses, and a slew of other devices, including micro-pumps, low-voltage micromotors, piezoelectric microphones, photoacoustic detectors, micromachined ultrasound transducers (pMUTs), robotic micro-legs, RF switches, and resonant scanners for high-definition projectors, are among the most promising high-volume. Because of their remarkable energy conversion efficiency between mechanical and electrical domains even on the microscale, piezoelectric materials are among the most suited materials in a variety of functional materials [12,13].

To put it another way, piezoelectric materials are very effective sensors and actuators, and their efficiency is independent of their size. MEMS devices are typically made up of facing electrodes, and lowering the gap distance can improve their sensitivity or actuator performance [14,15]. In contrast, using piezoelectric materials between electrodes can considerably improve sensitivity or actuation, comparable to capacitors, demonstrating that using functional materials can dramatically improve the performance of microscale devices.

There are a lot of parameters are used for analyzing the performance of piezoelectric cantilever beams such as Q-factor and electro-mechanical coupling coefficient (EMCC). The quality factor, often known as the Q factor, is a dimensionless parameter used in physics and engineering to indicate how well an oscillator or resonator is dampened. Generally, the Q-factor is estimated based on the frequencies which are obtained from the investigation process. When the Q-factor value is increased, the performance of the device also increases. The efficiency with which a piezoelectric material (or a device using one) transforms the energy in an imposed electrical signal to mechanical energy, or vice versa, is measured by the electromechanical coupling coefficient.

Based on the above discussion, the proposed work is designed for four piezoelectric cantilever beams to investigate the resonance frequency, Q-factor, EMCC, and output voltage. In this work, the geometry of previous literature [26] is used for both PZT-8 and AlN materials with coating of Al_2O_3 and parylene C. The simulation in air and water is performed in COMSOL Multiphysics and the results are compared for both piezoelectric materials used in air and water.

2. Materials and Methods

The design parameters of this work are considered from the previous literature [26] which is developed for the application of a piezoelectric xylophone transducer. This work executes the same dimensions with different piezoelectric materials to evaluate the best material with a better frequency level for the application of a piezoelectric xylophone transducer. In the literature work, the AlN material was employed as piezoelectric material. The structure formation of that work had five layers which includes two AlN layers with 1.5 μm and three Ti/Pt electrode layers with 15/30 nm. The lengths of the piezoelectric beam were taken

between the range of 200 μm to 245 μm to tune the fluid-loaded resonances to be in the range of 20 kHz – 40 kHz. The width of the beam was considered as 400 μm and placed with 100 μm space between each beam. This work employed a similar structure formation with an additional four layers. Over the top and bottom electrodes, Al₂O₃ is coated as a substrate material for 0.25 μm . After this layer, the perylene C is coated with 2 μm to improve the waterproofing and durability of the device. Moreover, Lead zirconate titanate (PZT-8) material is utilized as piezoelectric material. The layer structure formation of the proposed model in the single beam is shown in figure 1.

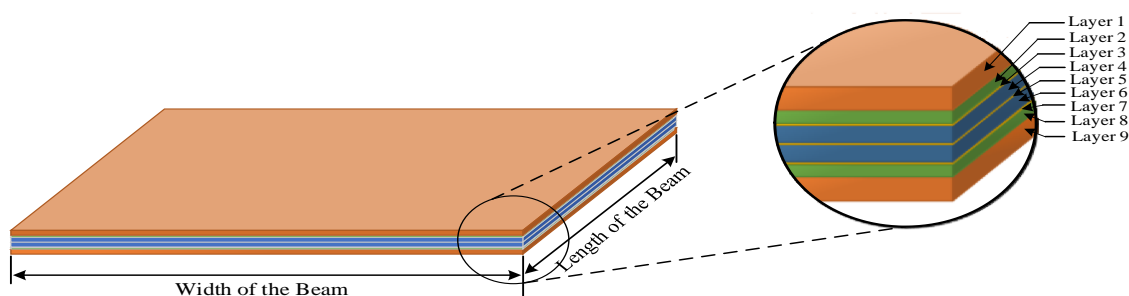


Figure 1. The layer structure formation of the proposed model.

The design parameters for four piezoelectric cantilever beams are given in table 1 along with the layer details.

Table 1. Design parameters and layer material details of the proposed model

Sl no	Length of the beam (μm)	Width of the beam (μm)	Material name/layer thickness								
			Layer 1	Layer 2	Layer 3	Layer 4	Layer 5	Layer 6	Layer 7	Layer 8	Layer 9
1	245	400	Parylene-C / 2 μm	Al ₂ O ₃ / 0.25 μm	Ti/Pt electrode / 15/30 nm	PZT-8 / 1.5 μm	Ti/Pt electrode / 15/30 nm	PZT-8 / 1.5 μm	Ti/Pt electrode / 15/30 nm	Al ₂ O ₃ / 0.25 μm	Parylene-C / 2 μm
2	226	400									
3	215	400									
4	200	400									

The deflection of the cantilever beam is estimated by utilizing Stoney's formula which is given in the following equation,

$$\partial = \frac{3\sigma(1-\nu) l^2}{E T^2} \quad (1)$$

Where the end reflection of the cantilever beam is expressed in ∂ , executed stress is represented in σ , the length of the beam is denoted in l , the thickness of the beam is described in T , Poisson's ratio of the material is denoted in ν , and the young's modulus of the material is expressed in E . The cantilever beam's movement depends on the thickness, width, length, and different material properties which are used for the beam structure. The materials used for

the beam and the shape of geometry are playing a significant role in discovering the stiffness of the cantilever beam. The following two equations are employed for estimating the mechanical and electrical behavior of the beam.

$$s = S_E \cdot P + D^T \cdot \varepsilon \quad (2)$$

$$d = D \cdot P + \epsilon_p \cdot \varepsilon \quad (3)$$

Where s defines the strain, d denotes the charge-density displacement, D includes the piezoelectric coefficient of the material, and ε represents the electric field interaction. The material properties of executed materials in this work are given in table 2.

Table 2. Material properties of utilized materials

Material properties	PZT-8	Parylene C	Al ₂ O ₃
Density (kg/m ³)	7600	1289	3965
Young's modulus (GPa)	63	2.8	400
Poisson's ratio	0.31	0.4	0.22
Relative permittivity	561.1	-	5.7
Coupling matrix (C/m ²)	10.3448	-	-

2.1 Energy Harvesting model

The piezoelectric cantilever beam is constructed with the help of figure 1 which consists of nine layers. The layer's details are shown in table 1 and the materials which are utilized for this work are

shown in table 2. One end of the beam is fixed and the other end is taken as free. This cantilever beam will deflect up and down while the force is applied at the free end. Due to this mechanical energy, electrical energy is generated as per figure 2.

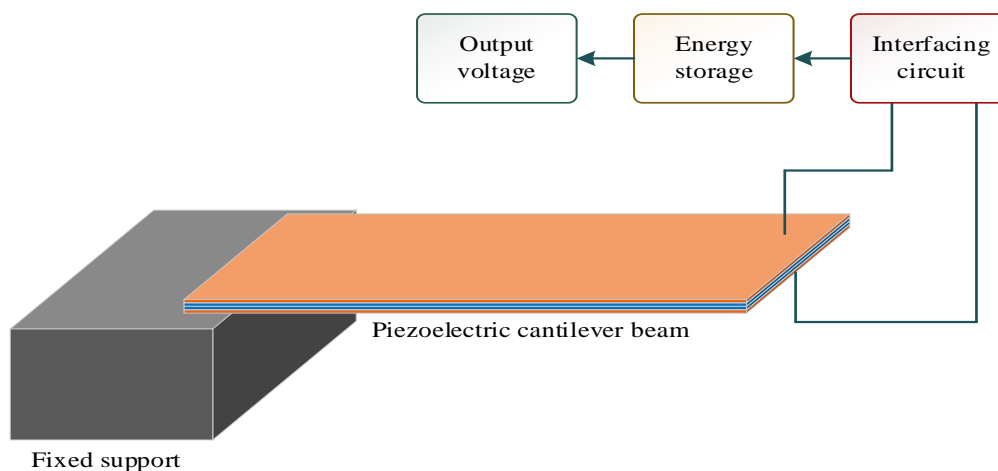


Figure 2. Energy Harvesting model.

In this model, the mechanical energy which results from the deflection of the beam is converted to electrical energy by using the interfacing circuit. The main application of the proposed work is to implant cochlear transducer. Therefore, the pressure value is given as the force for the piezoelectric beam. The following flow chart (in figure 3) is illustrating the procedures to design the piezoelectric cantilever beam geometry.

2.2 Modelling and Simulation

The modeling and simulation process is performed on the platform of COMSOL Multiphysics 5.6. The proposed work is using a 2D model of a piezoelectric cantilever beam for the analysis of mechanical and electrical properties. Acoustic-Piezoelectric interaction physics is executed for the proposed work with frequency-domain study. This physics model includes the pressure acoustic model, solid mechanics model, and electrostatics model. The design of this work is developed by using the geometry option. Here, six layers developed except the electrode layer because COMSOL doesn't require assigning any materials for electrodes. The materials are selected from the material library and the parylene C material is created with the help of blank material which is taken from [27]. The properties for parylene C are assigned as per the values which are given in table 2.

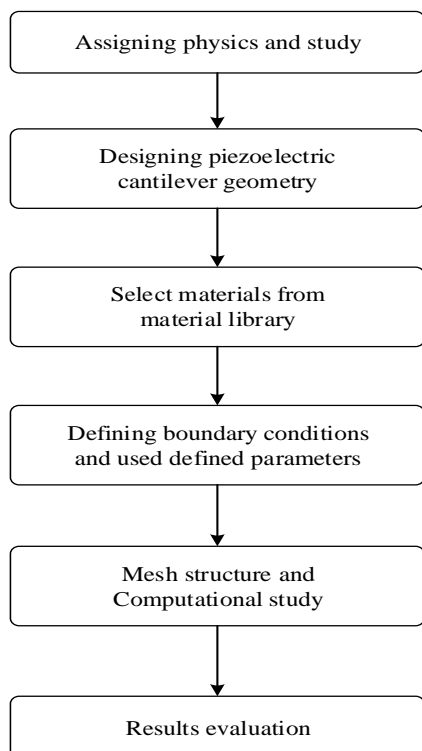


Figure 3. Flow chart for the procedure of beam geometrical design.

The proposed cantilever beams are simulated in two environments such as water and air. In the pressure acoustic model, the water or air domain is selected as pressure acoustic. The outer boundary of the water or air domain is selected as a sound-hard boundary (wall). In the solid mechanics model, all beam domains are assigned as solids and PZT-8 layers are assigned as piezoelectric material. The damping factor is selected from the linear elastic material and the damping type is chosen as the isotropic loss factor. The damping loss factor value is set as 0.001 for all simulations. One end of the beam is assigned as a fixed constraint and another end is assigned as a boundary load. The

load type is set to pressure to give the sound pressure as the input load. The sound pressure value for the water domain is $1 \mu\text{Pa}$ which is the reference sound pressure of water. For the air domain, $20 \mu\text{Pa}$ is given as a sound pressure which is the reference sound pressure value of air. In the electrostatic model, the piezoelectric material zone is chosen as the charge conversion of piezoelectric. The line between Al_2O_3 to PZT-8 is assigned as float potential to estimate the output voltage from the deflection and the middle line between two PZT-8 layer is assigned as a ground plane. After the assigning process, mesh properties are developed with the sequence type of physics-controlled mesh and the element size is set to normal. The mesh is formed in the shape of a triangular with a minimum element size of $0.15 \mu\text{m}$ to a maximum element size of $33.5 \mu\text{m}$. The maximum mesh growth rate is considered as 1.3 and the curvature factor of the mesh is taken as 0.3. The frequency range for the

all-piezoelectric beam is set as 10 kHz to 100 kHz for both water and air domains. Thereafter, the computation process is started to estimate the output voltage and resonance frequency. The graphs are plotted using a 1D plot with a point graph to validate the displacement of the beam, output voltage, and sound pressure level in acoustic domains. After the computation process, the resonance frequency is taken from the graph and the Q-factor is calculated by utilizing the following equation,

$$Q - \text{factor} = \frac{f_r}{f_a - f_r} \quad (4)$$

Where, f_r is representing the resonance frequency and f_a is expressing the anti-resonance frequency which is acquired from the graphs. The sample graph for discovering the resonance and anti-resonance frequencies is illustrated in figure 4.

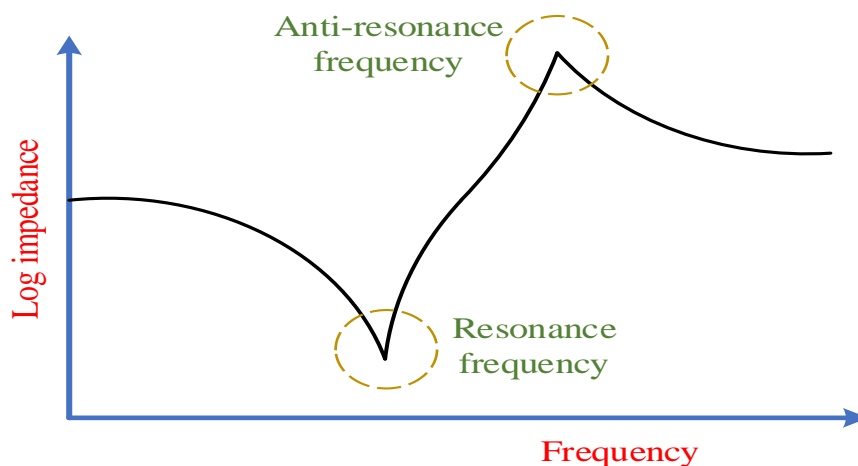


Figure 4. Sample graph for discovering resonance and anti-resonance frequencies

The resonance and antiresonance frequencies are obtained with the help of discovering the impedance value. To estimate the impedance value, the output current is calculated with the help of the following equation,

$$I = \int C * w * \delta \quad (5)$$

Where current is represented by I , surface charge density is expressed in C , angular frequency is denoted as δ , and w is the width of the beam. Furthermore, the following equation is used for calculating the impedance value.

$$Z = \frac{V}{\text{abs}(I)} \quad (6)$$

Where, impedance is denoted in Z , V representing the voltage output, and $\text{abs}(I)$ denoting the absolute value of current I . Moreover, the

electromechanical coupling coefficient (k) was also estimated with the help of the following equation,

$$k = \sqrt{\frac{(f_a^2 - f_r^2)}{f_a^2}} \quad (7)$$

3. Results and discussions

This section discusses the outcome of the proposed model in both water and air environment. The analysis process is performed on the platform COMSOL 5.6. The direct piezoelectric effect is applied over four various cantilever beams to investigate the displacement and output voltage. Moreover, the sound pressure level in both water and air environment are also analyzed. The acquired results are illustrated and explained in the following sections.

Water Environment

The proposed model is developed in terms of 2D geometry with the environment of water. The

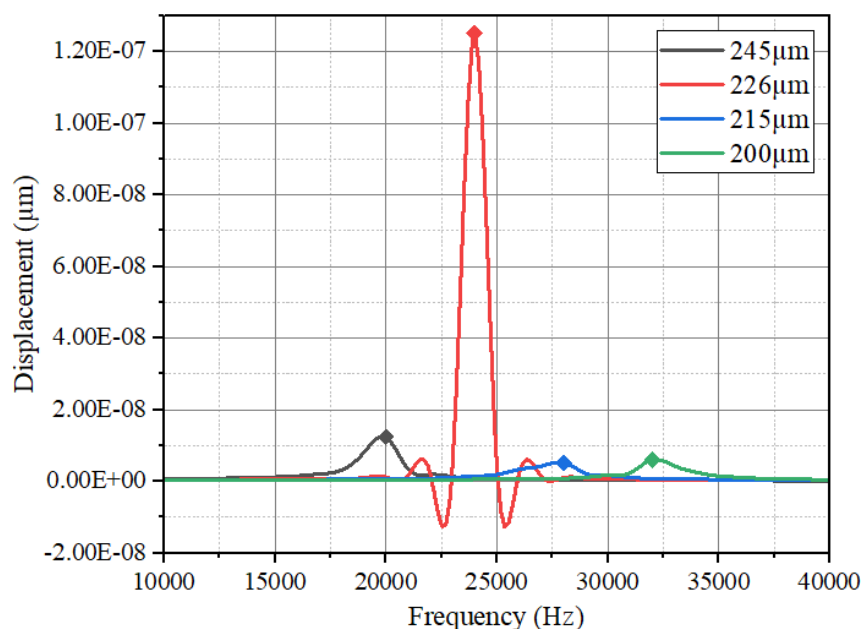
obtained resonance frequency, Q-factor, and EMCC for the proposed model are given in table 3.

Table 3. Obtained values for proposed model in water environment

Beam length (μm)	Resonance frequency (f_r) (kHz)	Q-factor	EMCC
245	19.03	19.51	0.31
226	23.97	22.19	0.29
215	26.97	24.97	0.28
200	31.99	31.36	0.25

As per the above-given table (table 3), the resonance frequency for the beam length of 245 μm is obtained as 19.03 kHz. The Q-factor value is acquired as 19.51 and EMCC is obtained as 0.31. For 226 μm beam length, a 23.97 kHz resonance frequency is attained, and a 22.19 Q-factor value is obtained. The EMCC for the beam length of 226 μm is acquired as 0.29. For 215 μm beam length,

resonance frequency, Q-factor, and EMCC are obtained as 26.97 kHz, 24.97, and 0.28 respectively. Similarly, the resonance frequency, Q-factor, and EMCC for 200 μm beam length are attained as 31.99 kHz, 31.36, and 0.25 respectively. The variation of displacement for different beam lengths is illustrated in figure 5.



Note: The peak displacement is marked with \blacklozenge in the diagram

Figure 5. Variation of displacement for different beam length

As per the above diagram (figure 5), the 245 μm beam length had achieved 1.24×10^{-8} μm displacement at 19.03 kHz frequency. In 226 μm beam length, the displacement is achieved as 1.25×10^{-7} μm at 23.97 kHz. Likewise, the displacement in the beam length of 215 μm is attained as 5.17×10^{-9} μm at the frequency of 26.97 kHz. For 200 μm

beam length, the obtained displacement is 6.03×10^{-9} at 31.99 kHz frequency. The displacement value is maximum for 226 μm beam length and minimum for 215 μm . The deformation of beams due to stress at their corresponding resonance frequency is illustrated in figure 6.

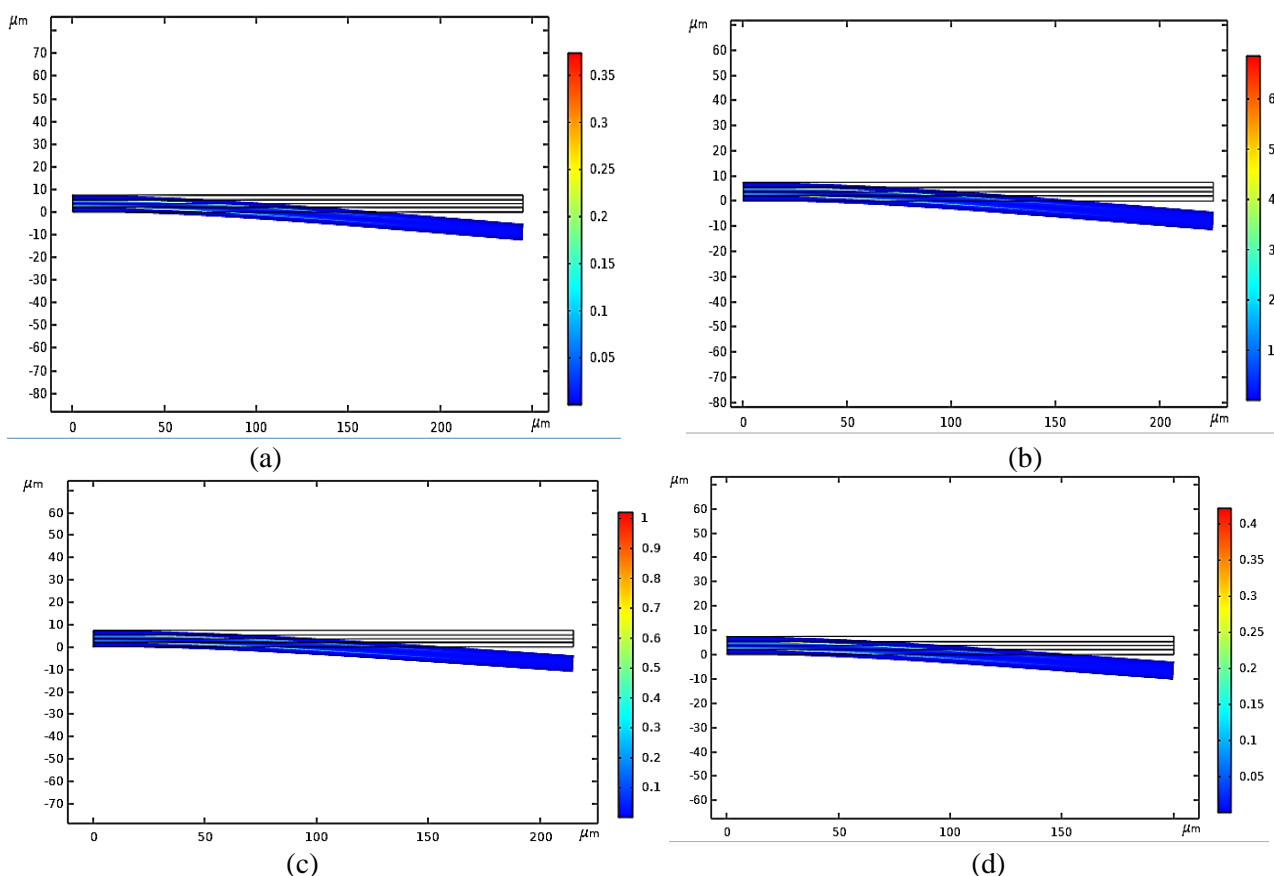


Figure 6. Deformation due to stress in various beam lengths in the water environment

In figure 6, the graphical representation in 6 (a) demonstrates the deformation in 245 μm beam length. Similarly, 6 (b), 6(c), and 6 (d) shows the graphical deformation of 226 μm, 215 μm, and 200 μm respectively. The color label shows the

variation of stress in Pa. As per the above graphical diagrams (in figure 6), maximum stress is acquired in the fixed end of the beams and minimum level of stress is acquired in the free end. Figure 7 illustrates the output voltage of various beam lengths.

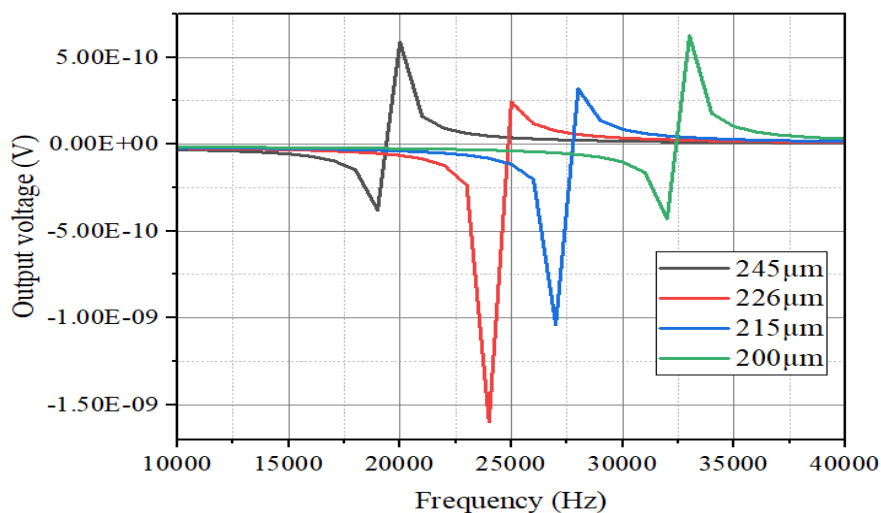


Figure 7. Obtained output voltage for different beam length

As per figure 7, the minimum voltage for beam lengths 245, 226, 215, and 200 μm are acquired as -3.79×10^{-10} , -1.6×10^{-9} , -1.04×10^{-9} , and -4.3×10^{-10} volts respectively. Similarly, the maximum

voltage is attained as 5.87×10^{-10} , 2.43×10^{-10} , 3.19×10^{-10} , and 6.24×10^{-10} volts respectively. The obtained SPL in a water environment for various beam lengths is demonstrated in figure 8.

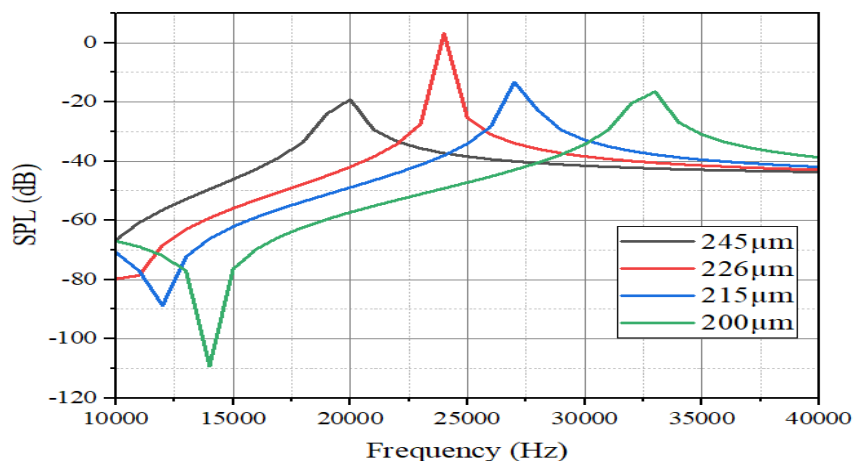


Figure 8. Obtained SPL for different beam length

In terms of figure 8, the SPL value for the beam lengths 245, 226, 215, and 200 μm are achieved as -19.12, 3.12, -13.31, and -16.53 dB respectively at their corresponding resonance frequencies. The

graphical representation of SPL in a water environment for the proposed beam lengths is shown in figure 9.

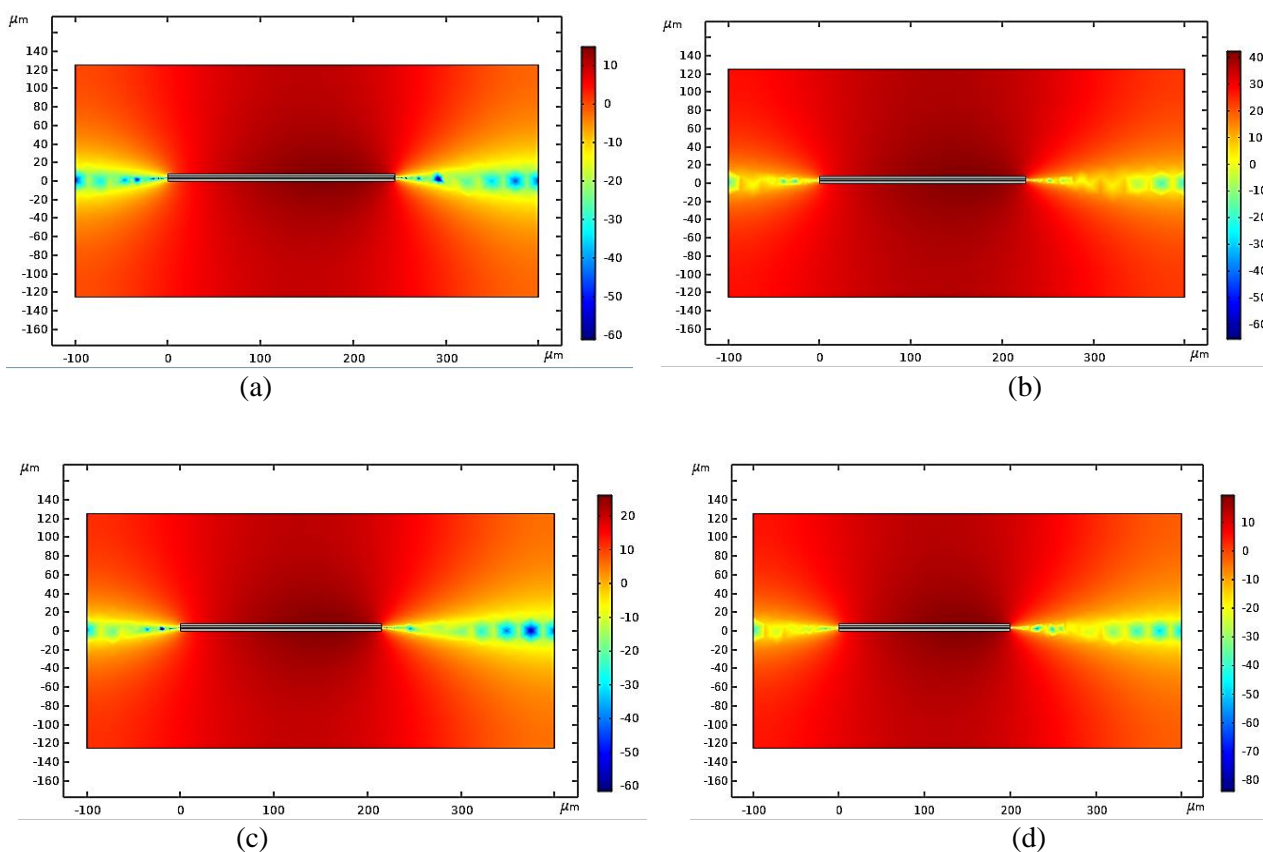


Figure 9. Graphical representation of SPL in various beam lengths in a water environment

In figure 9, the graphical representation in 9 (a), 9 (b), 9 (c), and 9 (d) are demonstrating the deformation in 245, 226, 215, and 200 μm beam lengths respectively. The color label in the

diagrams is denoting the variation of SPL in dB. The beam deflections when feeding 20 kHz as resonance frequency to the assembled proposed model are illustrated in figure 10.

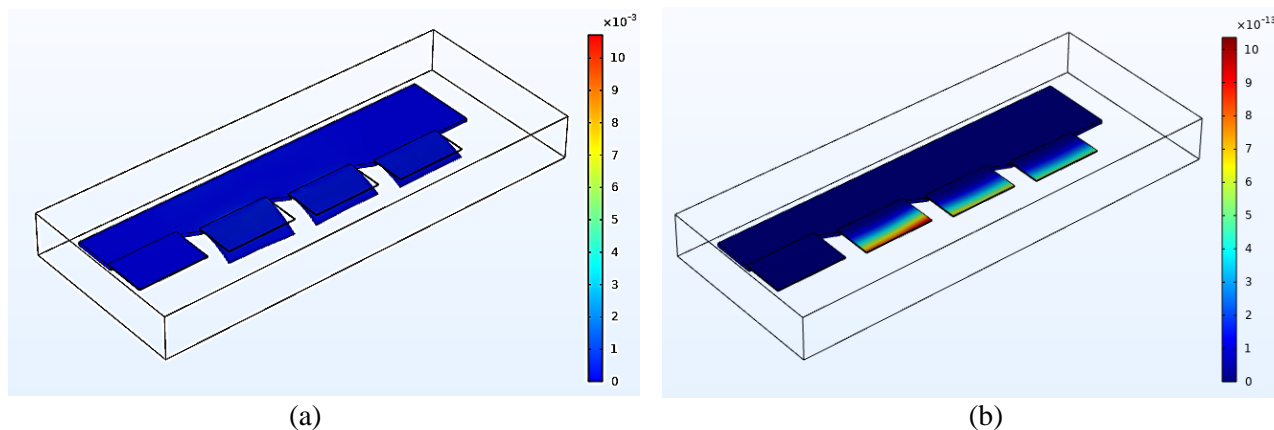


Figure 10. Graphical representation of beam deflections due to stress (a) and displacement (b) in water

The above graphical representation (figure 10) illustrates the deflection and displacement when feeding 20 kHz as a resonance frequency. Figure 10 (a) shows the deflection due to stress and color labels show the stress variation in Pa. Similarly, figure 10 (b) shows the displacement area and the color labels are denoting the variation of displacement in mm. In terms of the above diagram (in figure 10), beam 2 has acquired high-level deformation when feeding 20 kHz as a resonance frequency. Beam 3 has achieved high-level

deformation when compared to beam 1 and beam 4 but a low level was achieved compared to beam 2. When compared to beam 1 and beam 4, beam 4 has attained a high-level deformation. The following section discusses the obtained results in an air environment.

Air environment

The acquired resonance frequency, Q-factor, and EMCC for the proposed beam lengths are given in table 4.

Table 4. Obtained values for the proposed model in an air environment

Beam length (µm)	Resonance frequency (f_r) (kHz)	Q-factor	EMCC
245	50.96	49.48	0.2
226	59.93	58.19	0.18
215	66.03	64.74	0.17
200	76.02	69.11	0.17

As per table 5, the resonance frequency for beam lengths 245, 226, 215, and 200 µm in an air environment are acquired as 50.96, 59.93, 66.03, and 76.02 kHz respectively. The Q-factor is computed as 49.48, 58.19, 64.74, and 69.11

respectively. Similarly, EMCC is estimated as 0.2, 0.18, 0.17, and 0.17 respectively. Obtained displacement in the air environment for proposed beam lengths is shown in figure 11.

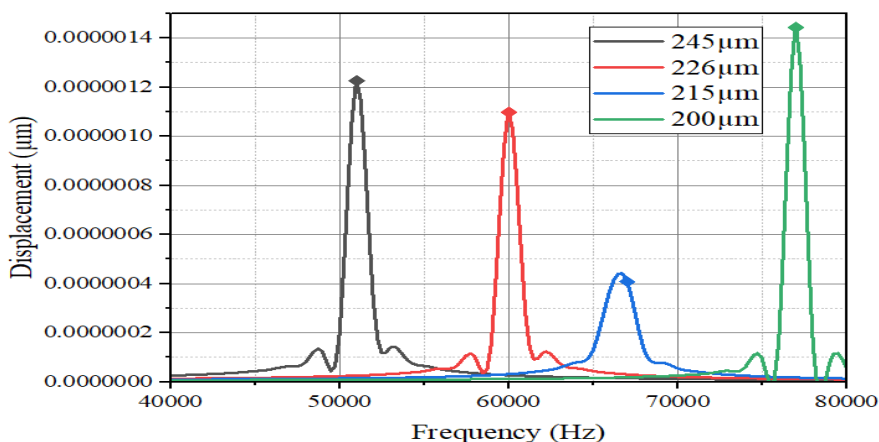


Figure 11. Variation of displacement for different beam length. The peak displacement is marked with ♦ in the diagram

In terms of the above graph (figure 11), the 245 µm beam length had attained 1.23×10^{-6} µm displacement at 50.96 kHz frequency. In 226 µm beam length, the displacement is acquired as 1.10

displacement at 50.96 kHz frequency. In 226 µm beam length, the displacement is acquired as 1.10

$\times 10^{-6} \mu\text{m}$ at 59.93 kHz. Likewise, the displacement in the beam length of 215 μm is obtained as $4.08 \times 10^{-7} \mu\text{m}$ at the frequency of 66.03 kHz. For 200 μm beam length, the acquired displacement is 1.44×10^{-6} at 76.02 kHz frequency. The displacement

value is maximum for 200 μm beam length and minimum for 215 μm . Figure 12 illustrates the deformation of beams due to stress at their corresponding resonance frequency.

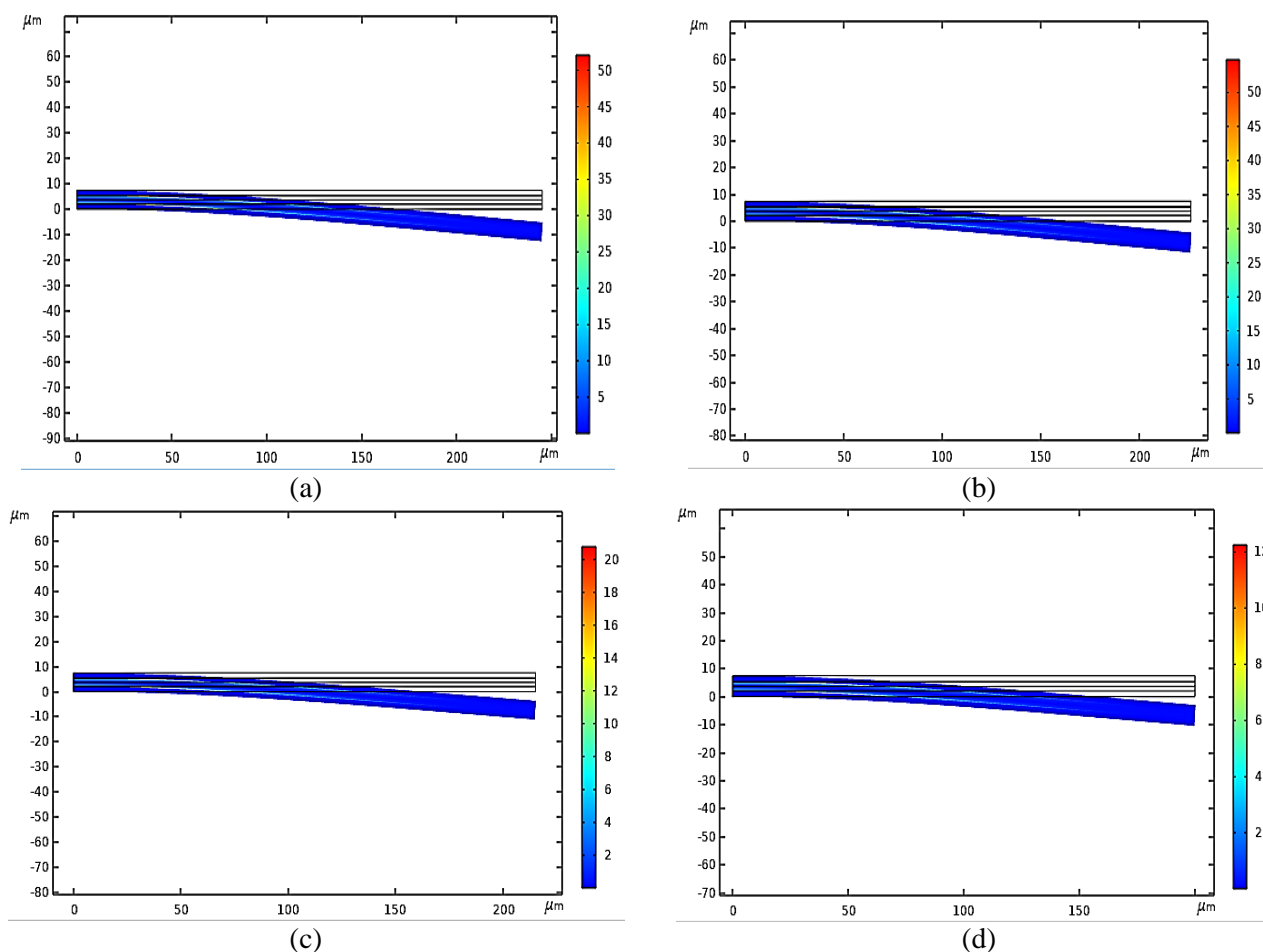


Figure 12. Deformation due to stress in various beam lengths in an air environment

In figure 12, the graphical representation in 6 (a), 6 (b), 6(c), and 6 (d) demonstrates the deformation in 245, 226, 215, and 200 μm beam length. The color label shows the variation of stress in Pa. As per the above graphical diagrams (in figure 12), maximum

stress is acquired in the fixed end of the beams and minimum level of stress is acquired in the free end. The output voltages of proposed beam lengths are plotted in figure 13.

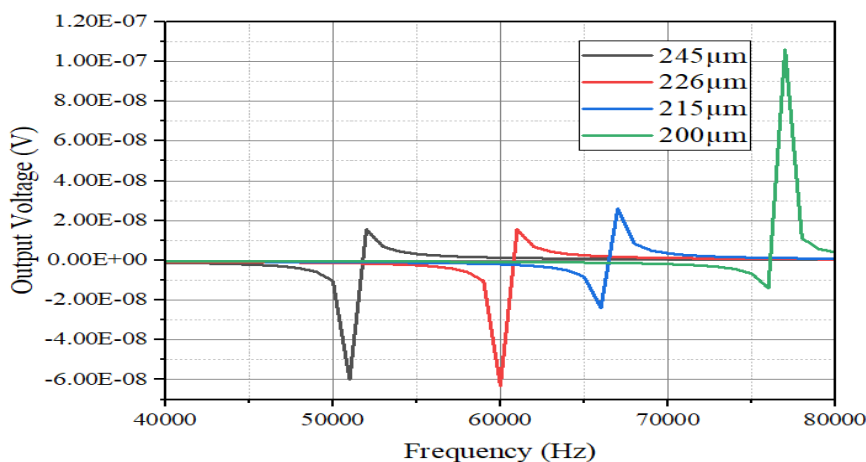


Figure 13. Obtained output voltage for the proposed beam length

As per figure 13, the minimum voltage for beam lengths 245, 226, 215, and 200 μm are acquired as -6.00×10^{-8} , -6.31×10^{-8} , -2.39×10^{-8} , and -1.4×10^{-8} volts respectively. Likewise, the maximum

voltage is attained as 1.56×10^{-8} , 1.54×10^{-8} , 2.59×10^{-8} , and 1.06×10^{-7} volts respectively. Figure 14 illustrates the obtained SPL in a water environment for various beam lengths.

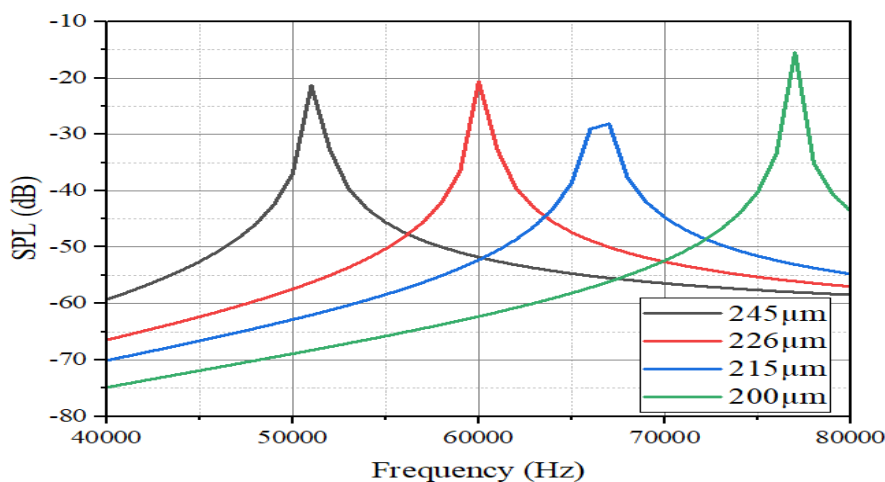


Figure 14. Obtained SPL for proposed beam lengths

In terms of figure 8, the SPL value for the beam lengths 245, 226, 215, and 200 μm are attained as -21.35, -20.67, -28.1, and -15.47 dB respectively at their corresponding resonance frequencies. Figure

15 demonstrates the graphical representation of SPL in a water environment for the proposed beam lengths.

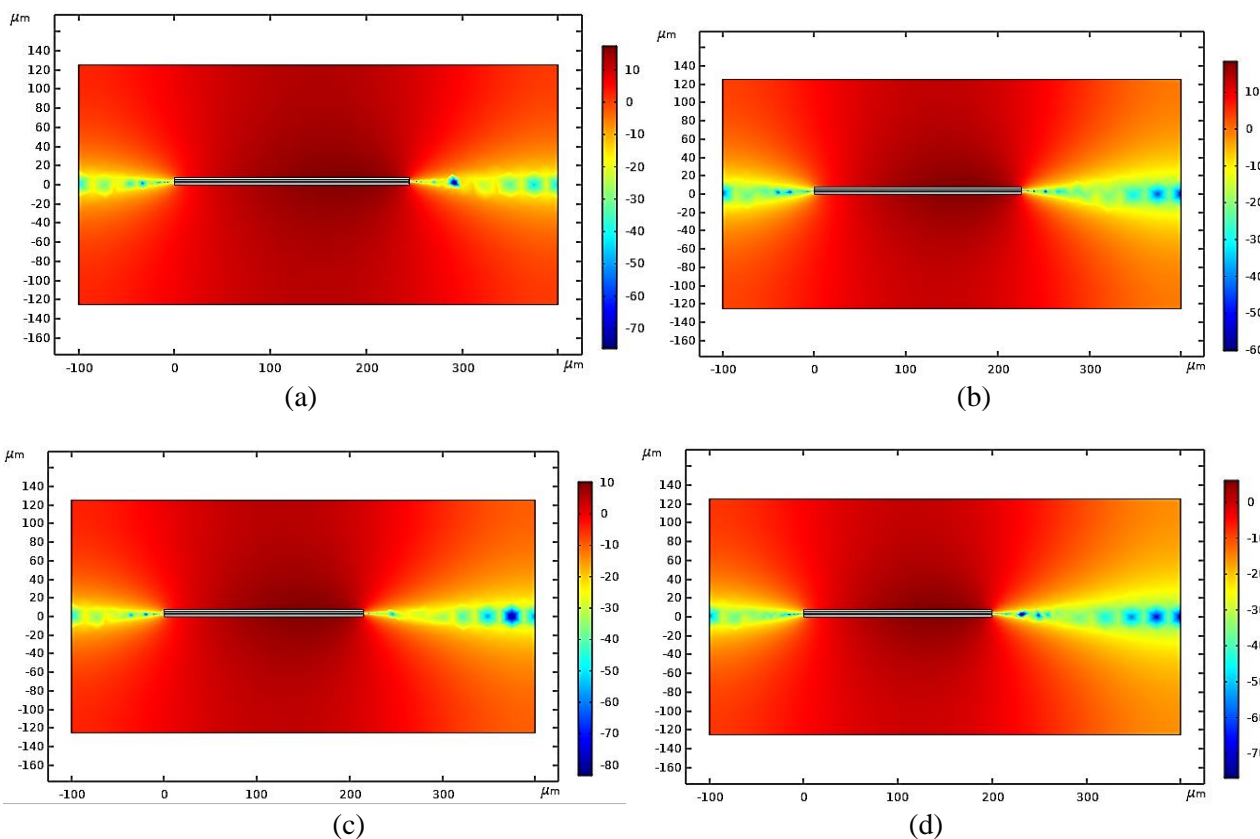


Figure 15. Graphical representation of SPL in various beam lengths in an air environment

In the above diagram (figure 15), the graphical representation in 15 (a), 15 (b), 15 (c), and 15 (d) are demonstrating the deformation in 245, 226, 215, and 200 μm beam lengths respectively. The

color label in the diagrams is denoting the variation of SPL in dB. The beam deflections when feeding 55 kHz as resonance frequency to the assembled proposed model are demonstrated in figure 16.

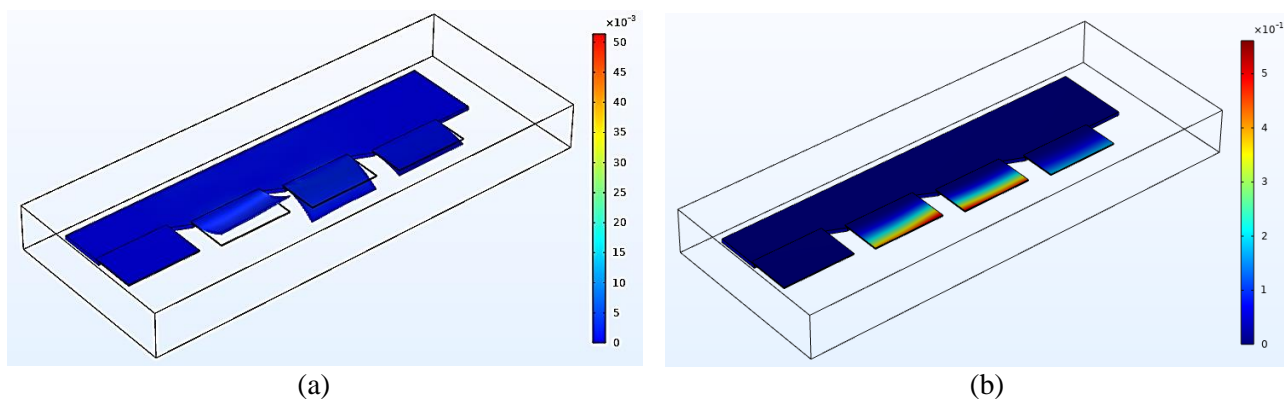


Figure 16. Graphical representation of beam deflections due to stress (a) and displacement (b) in air

The above graphical representation (figure 16) demonstrates the deflection and displacement when feeding 55 kHz as a resonance frequency. Figure 16 (a) denoting the deflection due to stress and color labels shows the stress variation in Pa. Similarly, figure 16 (b) illustrates the displacement area and the color labels are denoting the variation of displacement in mm. As per the above diagram (in figure 16), beam 2 has acquired maximum deformation when feeding 55kHz as a resonance frequency. Beam 3 has achieved maximum deformation when compared to beam 1 and beam 4 is still minimum to beam 2. When compared to beam 1 and beam 4, beam 4 has attained maximum

deformation. Further section conducting the comparative analysis of proposed work with existing and AlN with coating.

3.1 Comparative analysis

This section compares the obtained proposed results with the existing results in [26]. The existing model uses AlN as a piezoelectric material and the proposed model utilizes PZT-8 as a piezoelectric material. The comparison between resonance frequency and Q-factor in both water and air environment is performed. The values of comparison for water and air are given in table 5 and table 6 respectively.

Table 5. The comparison of resonance frequency and Q-factor in the water environment

Beam length (μm)	AlN (Existing) in water		AlN (with coating) in water		PZT-8 (Proposed) in water	
	Resonance frequency (kHz)	Q-factor	Resonance frequency (kHz)	Q-factor	Resonance frequency (kHz)	Q-factor
245	25.5	6.8	26.03	16.37	19.025	19.51
226	30.7	8.3	31.79	20.91	23.97	22.19
215	35.3	8.6	35.89	22.72	26.97	24.97
200	41.5	9.1	42.85	28.76	31.99	31.36

Table 6. The comparison of resonance frequency and Q-factor in an air environment

Beam length (μm)	AlN (Existing) in air		AlN (with coating) in air		PZT-8 (Proposed) in water	
	Resonance frequency (kHz)	Q-factor	Resonance frequency (kHz)	Q-factor	Resonance frequency (kHz)	Q-factor
245	86.2	42.2	87.95	46.53	50.96	49.48
226	101.3	113.2	102.75	54.37	59.93	58.18
215	112.5	60.9	113.77	59.26	66.03	64.74
200	129.5	68.7	131.79	66.23	76.02	69.11

As per table 5, the resonance frequency in the proposed model beam lengths 245, 226, 215, and 200 μm has reduced compared to the existing model in water. Likewise, the Q-factor was also enhanced when using the proposed model. As per table 6, the resonance frequency in the air is also

reduced compared to the existing model. Furthermore, the Q-factor also improved while using the proposed model. The comparison values of resonance frequency in the water environment are plotted as a bar diagram and shown in figure 17.

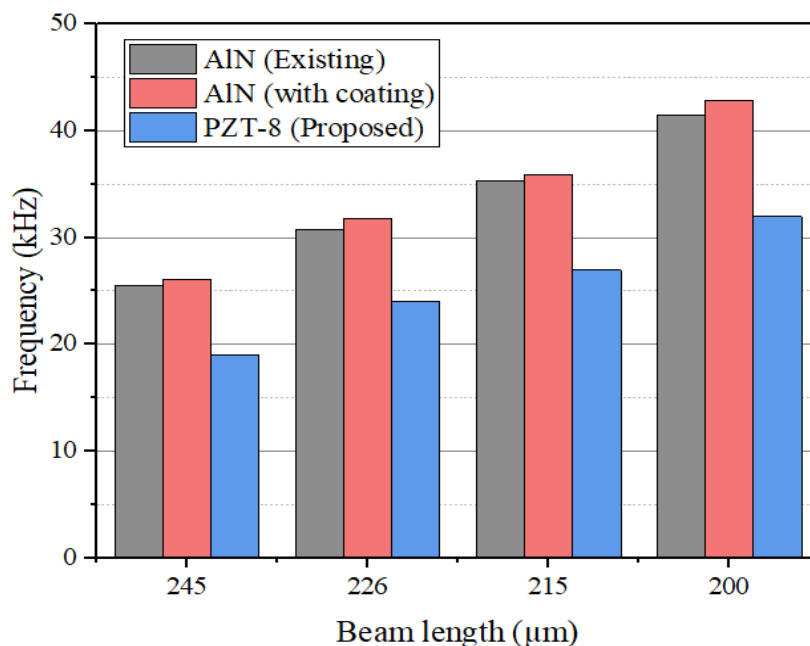


Figure 17. Bar diagram for the comparison of resonance frequency in water

In terms of the above diagram (figure 17), the resonance frequency for beam lengths 245, 226, 215, and 200 μm are reduced when compared to the existing work with the percentage of 25.39 %, 21.92 %, 23.59 %, and 22.92 % respectively.

Furthermore, 26.91%, 24.6%, 24.85%, and 25.34% respectively reduced when compared to the AlN with coating. Figure 18 demonstrates the comparison values of resonance frequency in an air environment.

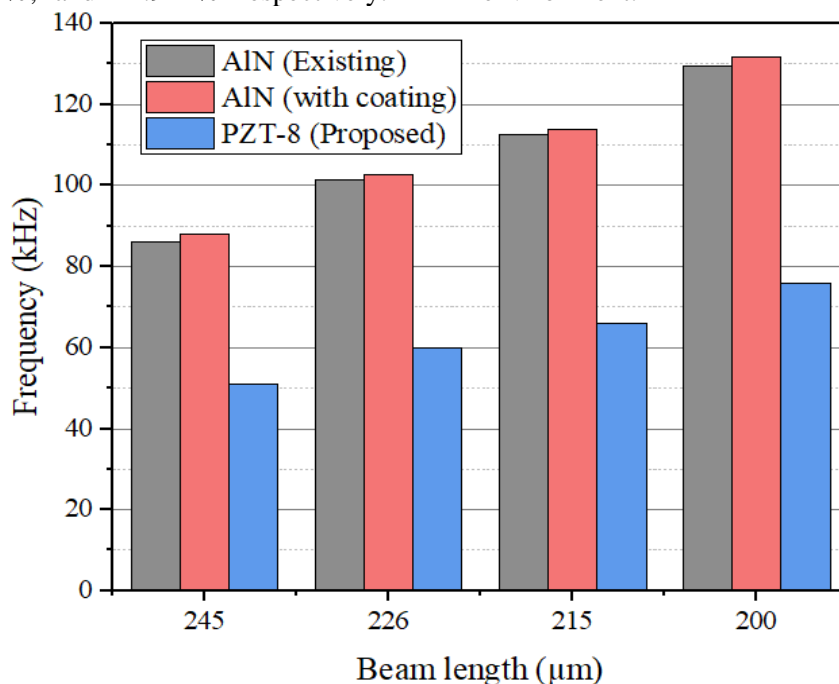


Figure 18. Bar diagram for the comparison of resonance frequency in air

As per the above diagram (figure 18), the resonance frequency for beam lengths 245, 226, 215, and 200 μm are also reduced in the air domain with the percentage of 40.88 %, 40.82 %, 41.31 %, and 41.3 % respectively when compared to the existing

work. Similarly, 42.06%, 41.67%, 41.96%, and 42.32% respectively reduced when compared to the AlN with coating. Figure 19 illustrates the comparison values of the Q-factor in a water environment.

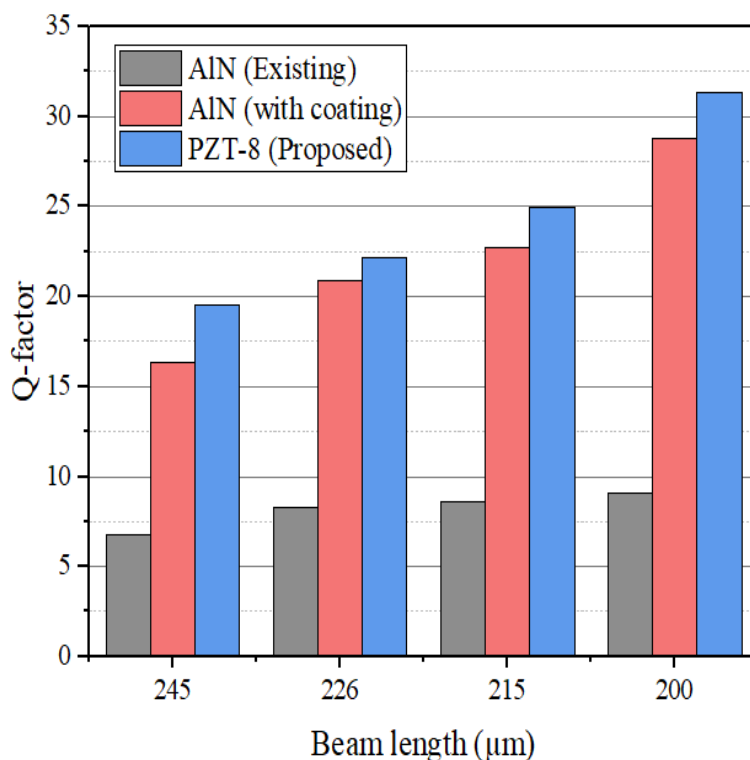


Figure 19. Bar diagram for the comparison of Q-factor in water

The above diagram (figure 19) shows the enhancement of the Q-factor in the proposed model compared to existing work with the percentage of 65.15 %, 62.6 %, 65.56 %, and 70.98 % for the beam length of 245, 226, 215, and 200 µm

respectively. When compared to the AIN with coating, the proposed PZT-8 is increased by 16.1%, 5.76%, 9.04%, and 8.3% respectively in terms of Q-factor. Similarly, the comparison bar diagram of the Q-factor in the air is shown in figure 20.

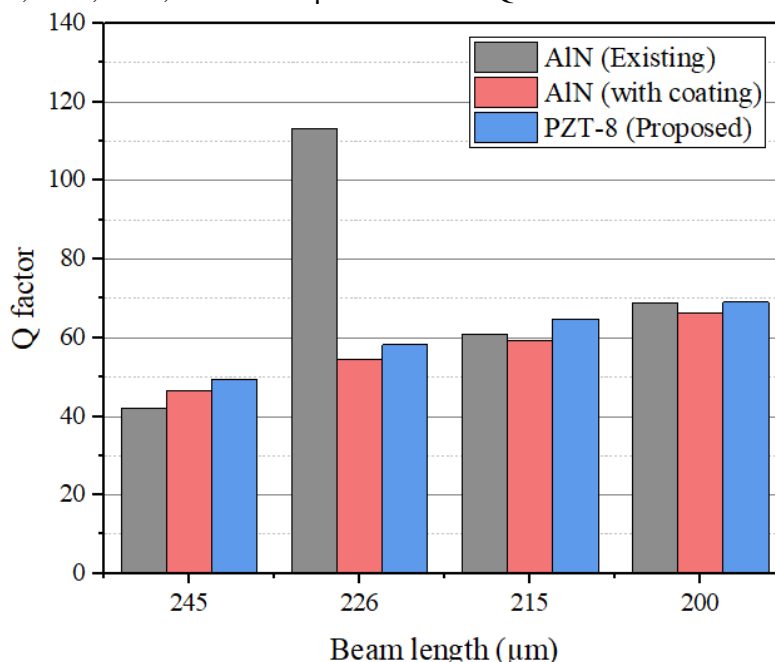


Figure 19. Bar diagram for the comparison of Q-factor in water

The above diagram (figure 19) shows the Q-factor in the proposed model is improved compared to existing work with the percentage of 14.71 %, 5.92 %, and 0.59 % for the beam length of 245, 215, and 200 µm respectively. Still, the beam length 226 Q-factor for the proposed model is reduced when

compared to the existing work with a percentage of 48.6 %. On another hand, the Q-factor of the proposed PZT-8 is increased by 5.95%, 6.56%, 8.47%, and 4.17% respectively when compared to AIN with coating. Overall, the proposed model with PZT-8 material performed well when

compared to the existing model with AlN material and AlN with coating.

In recent decades, extensive research has been conducted to develop piezoelectric cantilever beams for various applications [16][17][18][19][20][21][22][23][24][25]. These studies have explored different fabrication techniques, materials, and designs to enhance the performance of piezoelectric devices.

Some researchers have focused on fabricating piezoelectric cantilevers using innovative micromachining processes, such as bulk micromachining of silicon substrates and plasma etching to release microcantilevers and beams [16]. Other studies have investigated the use of specific piezoelectric materials, including Aluminum Nitride [17], ZnO [18][19][22], and BaTiO₃ [21][24][25], to optimize the energy harvesting and sensing capabilities of the devices.

Furthermore, researchers have explored diverse applications of piezoelectric cantilever beams. These applications include low-frequency vibration sensing and energy harvesting [16][17][18][19], artificial cochlear electrode arrays [20], photoelectrochemical systems [21][22], simultaneous temperature and pressure sensing [23], photocatalytic hydrogen generation [24], and bone scaffold cell responsiveness [25]. These investigations demonstrate the versatility of piezoelectric cantilever technology and its potential impact in various fields.

The presented paper focused on the design and analysis of a piezoelectric-based microbeam structure using PZT-8 as the piezoelectric material. The study aimed to investigate the resonance frequency, quality factor (Q-factor), electromechanical coupling coefficient (EMCC), displacement, stress, and output voltage of the proposed microbeam structure in both water and air environments. Additionally, a comparative analysis was conducted to evaluate the performance of the proposed model against an existing model that utilized AlN as the piezoelectric material and AlN with coating.

The results obtained from the experiments and simulations demonstrated the effectiveness of the proposed model. In terms of resonance frequency and Q-factor, the proposed PZT-8 microbeam exhibited favorable characteristics. Comparing the results with the existing AlN-based model, it was evident that the proposed model offered improved resonance frequencies and Q-factors in both water and air environments.

Furthermore, the displacement analysis indicated that the proposed model achieved varying levels of displacement for different beam lengths. Notably, the 200 μm beam length exhibited the highest displacement, while the 215 μm beam length had the lowest displacement. These findings provide valuable insights into the behavior and performance of the microbeam structure.

The stress analysis revealed that the maximum stress was acquired at the fixed end of the beams, while the minimum stress was observed at the free end. This distribution of stress can influence the structural integrity and durability of the microbeam, highlighting the importance of stress analysis in the design process.

The output voltage analysis demonstrated the electrical response of the proposed microbeam structure. The obtained results showed the range of voltage generated by the different beam lengths, with the 200 μm beam length producing the highest output voltage and the 215 μm beam length generating the lowest. These voltage measurements provide valuable information for potential applications of the microbeam structure in sensing and actuation systems.

The comparative analysis between the proposed model and the existing AlN-based model revealed the advantages of utilizing PZT-8 as the piezoelectric material. The proposed model exhibited reduced resonance frequencies and improved Q-factors in both water and air environments compared to the existing models. This suggests that the proposed PZT-8 microbeam structure has superior performance characteristics, making it a promising choice for various applications.

The discussion also highlighted the potential applications of the proposed model, including implant cochlear, piezoelectric acoustic transducers, microphones, and pressure sensors. These applications can benefit from the optimized characteristics of the proposed microbeam structure, such as enhanced resonance frequency, improved sensitivity, and increased efficiency.

4. Conclusion

The study successfully designed and analyzed a piezoelectric-based microbeam structure using PZT-8 as the piezoelectric material. The obtained results demonstrated the effectiveness and advantages of the proposed model over existing models. The findings contribute to the understanding of microbeam behavior and

performance in different environments. The potential applications highlighted in the discussion further emphasize the practical significance of the proposed model in various fields. Future research can explore additional aspects of the microbeam structure, such as its dynamic response and further optimizations to improve its performance in specific applications.

Reference

1. Keshavarzi, M. and Yavand Hasani, J., 2019. Design and optimization of fully differential capacitive MEMS accelerometer based on surface micromachining. *Microsystem Technologies*, 25(4), pp.1369-1377.
2. Sivasundari, K., Sugantharathnam, D.M. and Daniel, R.J., 2019. Fabrication of surface micromachined molybdenum cantilever beams for PWM MEMS pressure sensor and issues that affect yield. *Microsystem Technologies*, 25(7), pp.2535-2545.
3. Kciuk, S., Krzystała, E., Męzyk, A. and Szmidt, P., 2021. The Application of Microelectromechanical Systems (MEMS) Accelerometers to the Assessment of Blast Threat to Armored Vehicle Crew. *Sensors*, 22(1), p.316.
4. Drouin, J.R. and Theodore, R.M., 2020. Leveraging interdisciplinary perspectives to optimize auditory training for cochlear implant users. *Language and Linguistics Compass*, 14(9), p.e12394.
5. Cui, J. and Zhao, Q., 2021. A High Performance Tactical-grade Monolithic Horizontal Dual-axis MEMS Gyroscope with Off-plane Coupling Suppression Silicon Gratings. *IEEE Transactions on Industrial Electronics*.
6. Liang, Z., Yan, C.F., Rtimi, S. and Bandara, J., 2019. Piezoelectric materials for catalytic/photocatalytic removal of pollutants: Recent advances and outlook. *Applied Catalysis B: Environmental*, 241, pp.256-269.
7. Ali, F., Raza, W., Li, X., Gul, H. and Kim, K.H., 2019. Piezoelectric energy harvesters for biomedical applications. *Nano Energy*, 57, pp.879-902.
8. Shi, J., Liu, S., Zhang, L., Yang, B., Shu, L., Yang, Y., Ren, M., Wang, Y., Chen, J., Chen, W. and Chai, Y., 2020. Smart textile-integrated microelectronic systems for wearable applications. *Advanced materials*, 32(5), p.1901958.
9. Özdemir, A.E., 2019. Circuit topology for piezoelectric transducers in a piezoelectric energy harvester. *IET Renewable Power Generation*, 13(12), pp.2105-2110.
10. Shirvanimoghaddam, M., Shirvanimoghaddam, K., Abolhasani, M.M., Farhangi, M., Barsari, V.Z., Liu, H., Dohler, M. and Naebe, M., 2019. Towards a green and self-powered Internet of Things using piezoelectric energy harvesting. *IEEE Access*, 7, pp.94533-94556.
11. Bußmann, A.B., Durasiewicz, C.P., Kibler, S.H.A. and Wald, C.K., 2021. Piezoelectric titanium based microfluidic pump and valves for implantable medical applications. *Sensors and Actuators A: Physical*, 323, p.112649.
12. Zhou, H., Zhang, Y., Qiu, Y., Wu, H., Qin, W., Liao, Y., Yu, Q. and Cheng, H., 2020. Stretchable piezoelectric energy harvesters and self-powered sensors for wearable and implantable devices. *Biosensors and Bioelectronics*, 168, p.112569.
13. Mokhtari, F., Azimi, B., Salehi, M., Hashemikia, S. and Danti, S., 2021. Recent advances of polymer-based piezoelectric composites for biomedical applications. *Journal of the Mechanical Behavior of Biomedical Materials*, 122, p.104669.
14. Hou, Y., Jiao, R. and Yu, H., 2021. MEMS based geophones and seismometers. *Sensors and Actuators A: Physical*, 318, p.112498.
15. Wang, H., Ma, Y., Yang, H., Jiang, H., Ding, Y. and Xie, H., 2020. MEMS ultrasound transducers for endoscopic photoacoustic imaging applications. *Micromachines*, 11(10), p.928.
16. Rashmi, K.R., Rao, A.S., Jayarama, A. and Pinto, R., 2019. Piezoelectric P (VDF-TrFE) micro cantilevers and beams for low frequency vibration sensors and energy harvesters. *Sensors and Actuators A: Physical*, 295, pp.574-585.
17. de Oliveira, F.A.C., de Lima Monteiro, D.W. and Colombo, D.M., 2021. Design, modeling, characterization and analysis of a low frequency micro-fabricated piezoelectric cantilever for vibration sensing and energy harvesting applications. *Sensors and Actuators A: Physical*, 326, p.112709.
18. Singh, R., Pant, B.D. and Jain, A., 2020. Simulations, fabrication, and characterization of d31 mode piezoelectric vibration energy harvester. *Microsystem Technologies*, 26(5), pp.1499-1505.
19. Saxena, S., Sharma, R. and Pant, B.D., 2019. Fabrication and comparison of guided two-beam and four-beam piezoelectric energy harvester for low-frequency operation. *Journal of Microelectromechanical Systems*, 28(3), pp.513-520.

20. Saadatzi, M., Saadatzi, M.N. and Banerjee, S., 2020. Modeling and fabrication of a piezoelectric artificial cochlea electrode array with longitudinal coupling. *IEEE Sensors Journal*, 20(19), pp.11163-11172.
21. Liu, Z., Wang, L., Yu, X., Zhang, J., Yang, R., Zhang, X., Ji, Y., Wu, M., Deng, L., Li, L. and Wang, Z.L., 2019. Piezoelectric-effect-enhanced full-spectrum photoelectrocatalysis in p-n heterojunction. *Advanced Functional Materials*, 29(41), p.1807279.
22. Zhang, S., Liu, Z., Ruan, M., Guo, Z., Lei, E., Zhao, W., Zhao, D., Wu, X. and Chen, D., 2020. Enhanced piezoelectric-effect-assisted photoelectrochemical performance in ZnO modified with dual cocatalysts. *Applied Catalysis B: Environmental*, 262, p.118279.
23. Song, K., Zhao, R., Wang, Z.L. and Yang, Y., 2019. Conjoined pyro-piezoelectric effect for self-powered simultaneous temperature and pressure sensing. *Advanced Materials*, 31(36), p.1902831.
24. Jiang, Y., Li, M., Mi, Y., Guo, L., Fang, W., Zeng, X., Zhou, T. and Liu, Y., 2021. The influence of piezoelectric effect on the heterogeneous photocatalytic hydrogen production of strontium titanate nanoparticles. *Nano Energy*, 85, p.105949.
25. Shuai, C., Liu, G., Yang, Y., Yang, W., He, C., Wang, G., Liu, Z., Qi, F. and Peng, S., 2020. Functionalized BaTiO₃ enhances piezoelectric effect towards cell response of bone scaffold. *Colloids and Surfaces B: Biointerfaces*, 185, p.110587.
26. Zhao, C., Knisely, K.E. and Grosh, K., 2018. Design and fabrication of a piezoelectric MEMS xylophone transducer with a flexible electrical connection. *Sensors and Actuators A: Physical*, 275, pp.29-36.
27. <https://vsiparylene.com/parylene-properties/>